

Superconductivity from the Condensation of Topological Defects in a Quantum Spin-Hall Insulator

Yuhai Liu,¹ Zhenjiu Wang,² Toshihiro Sato,² Martin Hohenadler,²

Chong Wang,³ Wenan Guo,^{1,4,*} and Fakhre F. Assaad^{2,†}

¹*Department of Physics, Beijing Normal University, Beijing 100875, China*

²*Institut für Theoretische Physik und Astrophysik, Universität Würzburg, Am Hubland, 97074 Würzburg, Germany*

³*Perimeter Institute for Theoretical Physics, Waterloo, Ontario, Canada N2L 2Y5*

⁴*Beijing Computational Science Research Center, Beijing 100193, China*

The discovery that spin-orbit coupling can generate a new state of matter in the form of quantum spin-Hall (QSH) insulators has brought topology to the forefront of condensed matter physics. While QSH states from spin-orbit coupling can be fully understood in terms of band theory, fascinating many-body effects are expected if the state instead results from interaction-generated symmetry breaking. In particular, topological defects of the corresponding order parameter provide a route to exotic quantum phase transitions. Here, we introduce a model in which the condensation of skyrmion defects in an interaction-generated QSH insulator produces a superconducting (SC) phase. Because vortex excitations of the latter carry a spin-1/2 degree of freedom numbers, the SC order may be understood as emerging from a gapless spin liquid normal state. The QSH-SC transition is an example of a deconfined quantum critical point (DQCP), for which we provide an improved model with only a single length scale that is accessible to large-scale quantum Monte Carlo simulations.

In the Kane-Mele model for the QSH insulator,¹ the original SU(2) spin symmetry is explicitly broken by spin-orbit coupling. Here, we instead consider the case where this symmetry is preserved by the Hamiltonian but spontaneously broken by an interaction-generated QSH state.² At the mean-field level, the latter is characterised by an SO(3) order parameter constant in space and time and a band structure with a non-trivial \mathbb{Z}_2 topological index.^{1,3,4} Long-wavelength fluctuations of this order parameter include in particular the Goldstone modes that play a key role for phase transitions to, e.g., a Dirac semimetal. Such a transition, illustrated in Fig. 1a, is described by a Gross-Neveu-Yukawa field theory⁵ with QSH order encoded in a mass in the underlying Dirac equation. Fluctuations can also take the form of topological ('skyrmion') defects that correspond to a nontrivial winding of the order parameter vector. Due to the topological nature of the QSH state itself, such skyrmions carry electric charge $2e$:⁶ as illustrated in the supplemental material, the insertion of a skyrmion in a system with open boundaries pumps a pair of charges from the valence to the conduction band through the helical edge states. The condensation of skyrmion defects—which coincides with the destruction of the QSH state—represents a new route to generate a SC state. In contrast to a weakly coupled Bardeen-Cooper-Schrieffer-type SC, its vortices enclose a spin-1/2 degree of freedom corresponding to the fractionalized QSH order parameter.⁶

A direct QSH-SC phase transition (Fig. 1a) is an instance of a DQCP,⁷⁻⁹ the concept of which relies on the topological defects of one phase carrying the *charge* of the

other phase. Defect condensation then provides a mechanism for a continuous transition between two states with different broken symmetries (SO(3) for QSH, U(1) for SC) that is forbidden by Landau theory. Despite considerable numerical efforts,^{10,11} DQCPs remain a subject of intense debate. Important questions include their very nature—weakly first order or continuous⁹—and the role of emergent symmetries.¹² One of the difficulties lies in the fact that previous lattice realizations^{11,13,14} involve antiferromagnetic (AFM) and valence bond solid (VBS) phases. For the widely studied square lattice, the VBS state breaks the discrete \mathbb{Z}_4 rotation symmetry, whereas the field theory has a U(1) symmetry. The latter is recovered on the lattice exactly at the critical point, but in general the \mathbb{Z}_4 symmetry breaking term is relevant. The additional length scale at which the \mathbb{Z}_4 symmetry becomes visible obscures the numerical analysis. In the field theory, this translates into the notion that quadruple skyrmion addition (monopole) events of the AFM SO(3) order parameter are irrelevant at criticality but proliferate slightly away from this point to generate the VBS state.⁷ Hence, the theory is subject to a dangerously irrelevant

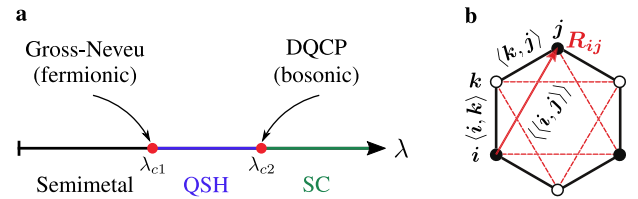


FIG. 1. **Phase diagram and model.** **a** Schematic ground-state phase diagram with semimetallic, QSH, and SC phases. **b** Illustration of nearest- and next-nearest neighbours and the vector \mathbf{R}_{ij} on a plaquette of the honeycomb lattice.

* waguo@bnu.edu.cn

† fakhre.assaad@physik.uni-wuerzburg.de

evant operator. This complication is completely avoided in the model introduced here, where the DQCP separates QSH and SC rather than AFM and VBS phases. QSH and AFM order are both described by an $\text{SO}(3)$ order parameter. However, instead of the \mathbb{Z}_4 symmetry broken by lattice VBS state, the SC phase breaks the same global $\text{U}(1)$ gauge symmetry (charge conservation) on the lattice and in the continuum. Therefore, the number of skyrmion defects with charge $2e$ is conserved and monopoles are absent.

The exciting prospects of (i) SC order from topological defects of a spontaneously generated QSH state and (ii) a monopole-free realisation of a DQCP motivate the search for a suitable lattice model amenable to quantum Monte Carlo simulations without a sign problem. Such efforts are part of the recent surge of designer Hamiltonians aimed at studying exotic phases and phase transitions.^{15–21} Here, we start from a tight-binding model of Dirac fermions in the form of electrons on the honeycomb lattice with nearest-neighbour hopping (see Fig. 1b), as described by

$$\hat{H}_t = -t \sum_{\langle i,j \rangle} (\hat{c}_i^\dagger \hat{c}_j + \text{H.c.}). \quad (1)$$

The spinor $\hat{c}_i^\dagger = (\hat{c}_{i,\uparrow}^\dagger, \hat{c}_{i,\downarrow}^\dagger)$, where $\hat{c}_{i,\sigma}^\dagger$ creates an electron at lattice site i with spin σ . Equation (1) yields the familiar graphene band structure with gapless, linear excitations at the Dirac points.²² A suitable interaction that generates the above physics is

$$\hat{H}_\lambda = -\lambda \sum_{\square} \left(\sum_{\langle\langle i,j \rangle\rangle \in \square} i\nu_{ij} \hat{c}_i^\dagger \boldsymbol{\sigma} \hat{c}_j + \text{H.c.} \right)^2. \quad (2)$$

The first sum is over all the hexagons of a honeycomb lattice with $L \times L$ units cells and periodic boundary conditions. The second sum is over all pairs of next-nearest-neighbour sites of a hexagon, see Fig. 1b. The quantity $\nu_{ij} = \pm 1$ is identical to the Kane-Mele model;¹ for a path from site i to site j (connected by \mathbf{R}_{ij} , see Fig. 1b) via site k , $\nu_{ij} = \hat{e}_z \cdot (\mathbf{R}_{ik} \times \mathbf{R}_{kj}) / |\hat{e}_z \cdot (\mathbf{R}_{ik} \times \mathbf{R}_{kj})|$ with \hat{e}_z a unit vector perpendicular to the honeycomb plane. Finally, $\boldsymbol{\sigma} = (\sigma^x, \sigma^y, \sigma^z)$ with the Pauli spin matrices σ^α . The rationale for this choice of interaction is easy to understand. Without the square, and taking just one of the three Pauli matrices, equation (2) reduces to the Kane-Mele spin-orbit coupling that explicitly breaks $\text{SO}(3)$ spin symmetry. In contrast, this symmetry is preserved by \hat{H}_λ but spontaneously broken by long-range QSH order. For $\lambda > 0$, the model defined by $\hat{H} = \hat{H}_t + \hat{H}_\lambda$ can be simulated without a sign problem by auxiliary-field quantum Monte Carlo methods.^{23–25} In the following, we set $t = 1$ and consider a half-filled band with one electron per site.

A mean-field decomposition of equation (2) suggests a transition from the Dirac semimetal to a QSH state at a critical value $\lambda_{c1} > 0$. However, it is highly non-trivial

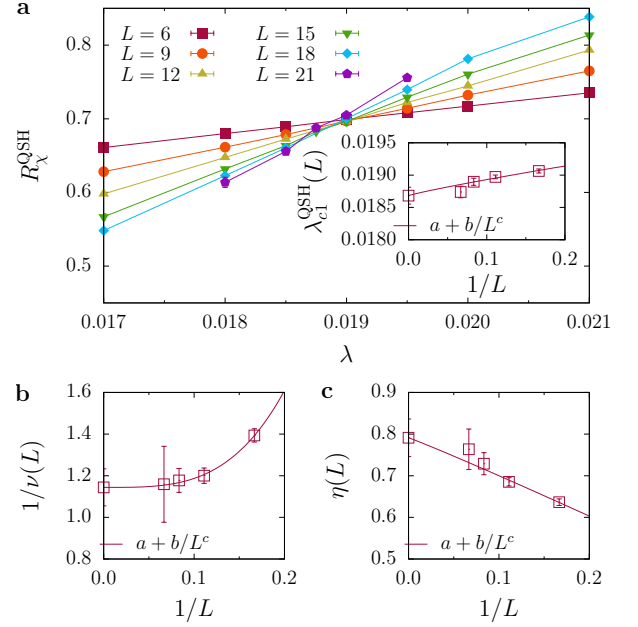


FIG. 2. Gross-Neveu semimetal-QSH transition. **a** Correlation ratio R_χ^{QSH} [equation (5)] for different system sizes L . The extrapolation of the crossing points of R_χ^{QSH} for L and $L+6$ in the inset gives the critical value $\lambda_{c1} = 0.0187(2)$. **b** Finite-size scaling based on equation (6) gives an inverse correlation length exponent $1/\nu = 1.14(9)$. **c** Estimation of the anomalous dimension $\eta = 0.79(5)$.

if the associated saddle point is stable. In fact, s-wave pair hopping processes arise upon expanding the square in equation (2) and can lead to superconductivity.²⁶ The exact phase diagram can be obtained by quantum Monte Carlo simulations. Remarkably, as illustrated in Fig. 1a, we find two distinct phase transitions. First, from the semimetal to a QSH state at λ_{c1} , then from the QSH state to an s-wave SC at $\lambda_{c2} > \lambda_{c1}$.

The semimetal-QSH transition involves the breaking of spin rotation symmetry and is expected to be in the $\text{O}(3)$ Gross-Neveu universality class for $N = 8$ Dirac fermions (two sublattices, two Dirac points, $\sigma = \uparrow, \downarrow$). The local vector order parameter takes the form of a spin current,

$$\hat{\mathcal{O}}_{\mathbf{r},\boldsymbol{\delta}}^{\text{QSH}} = i\hat{c}_{\mathbf{r}}^\dagger \boldsymbol{\sigma} \hat{c}_{\mathbf{r}+\boldsymbol{\delta}} + \text{H.c.}, \quad (3)$$

where \mathbf{r} corresponds to a unit cell labelling a hexagon, and $\mathbf{r} + \boldsymbol{\delta}$ runs over all next-nearest neighbours. Because this order parameter is a lattice regularisation of the three QSH mass terms in the Dirac equation, long-range order implies a mass gap.¹ To study the phase transition, we computed the associated susceptibility

$$\chi_{\boldsymbol{\delta},\boldsymbol{\delta}'}^{\mathcal{O}}(\mathbf{q}) = \frac{1}{L^2} \sum_{\mathbf{r},\mathbf{r}'} \int_0^\beta d\tau e^{i\mathbf{q} \cdot (\mathbf{r}-\mathbf{r}')} \langle \hat{\mathcal{O}}_{\mathbf{r},\boldsymbol{\delta}}(\tau) \hat{\mathcal{O}}_{\mathbf{r}',\boldsymbol{\delta}'}(0) \rangle. \quad (4)$$

Here, we omitted the vanishing background term and concentrate on the largest eigenvalue of $\chi_{\boldsymbol{\delta},\boldsymbol{\delta}'}^{\mathcal{O}}(\mathbf{q})$ (see sup-

plementary material), henceforth denoted as $\chi^O(\mathbf{q})$. To detect the transition, we consider the renormalization-group invariant correlation ratio

$$1 - \frac{\chi^O(\mathbf{Q} + \Delta\mathbf{q})}{\chi^O(\mathbf{Q})} = R_\chi^O \left(L^{1/\nu} (\lambda - \lambda_c^O), L^{-w} \right) \quad (5)$$

with $|\Delta\mathbf{q}| = \frac{4\pi}{\sqrt{3}L}$, the ordering wavevector $\mathbf{Q} = 0$, the correlation length exponent ν , and the leading corrections-to-scaling exponent w . We set the inverse temperature $\beta = L$ in our simulations based on the assumption of a dynamical critical exponent $z = 1$.²⁷ In contrast to previous analyses of Gross-Neveu criticality^{28,29} we use susceptibilities rather than equal-time correlators to suppress background contributions to the critical fluctuations.

The results for the semimetal-QSH transition are shown in Fig. 2. The finite-size estimate of the critical value, $\lambda_{c1}^{\text{QSH}}(L)$, corresponds to the crossing point of R_χ^{QSH} for L and $L + 6$. Extrapolation to the thermodynamic limit (inset of Fig. 2a) yields $\lambda_{c1}^{\text{QSH}} = 0.0187(2)$. As shown in the supplementary material, the single-particle gap is nonzero for $\lambda > \lambda_{c1}^{\text{QSH}}$. The correlation length exponent was estimated from¹⁰

$$\frac{1}{\nu^O(L)} = \frac{1}{\log r} \log \left(\frac{\frac{d}{d\lambda} R_\chi^O(\lambda, rL)}{\frac{d}{d\lambda} R_\chi^O(\lambda, L)} \right) \bigg|_{\lambda=\lambda_c^O(L)} \quad (6)$$

with $r = \frac{L+6}{L}$. A similar equation can be used to determine the exponent η from the divergence of the susceptibility ($\chi^O \propto L^{2-\eta}$) at criticality (see supplementary material). Aside from a polynomial interpolation of the data as a function of λ for each L , this analysis does not require any further fitting and, by definition, converges to the correct exponents in the thermodynamic limit with rate L^{-w} . While previous estimates of the critical exponents vary,^{28–30} the values $1/\nu = 1.14(9)$ and $\eta = 0.79(5)$ from Fig. 2 are consistent with $\nu = 1.02(1)$ and $\eta = 0.76(2)$ from previous work.²⁹ This suggests that the semimetal-QSH transition is in the same universality class as the semimetal-AFM transition.^{28,29,31}

To detect SC order, we used the order parameter

$$\hat{O}_{\mathbf{r},\tilde{\mathbf{d}}}^{\text{SC}} = \frac{1}{2} \left(\hat{c}_{\mathbf{r}+\tilde{\mathbf{d}},\uparrow}^\dagger \hat{c}_{\mathbf{r}+\tilde{\mathbf{d}},\downarrow}^\dagger + \text{H.c.} \right) \quad (7)$$

where $\mathbf{r} + \tilde{\mathbf{d}}$ runs over the two orbitals of unit cell \mathbf{r} . As before, we computed the corresponding susceptibility and used $\beta = L$ in anticipation of $z = 1$. Fig 3 shows that, within the very small error bars, the critical value for SC order $\lambda_{c2}^{\text{SC}} = 0.0332(2)$ and the critical value for the disappearance of long-range QSH order $\lambda_{c2}^{\text{QSH}} = 0.03322(3)$ are identical, suggesting a direct QSH-SC transition. At this transition, the single-particle gap remains of order one and we find no evidence for a first-order transition for the available system sizes (supplementary Fig. 2).

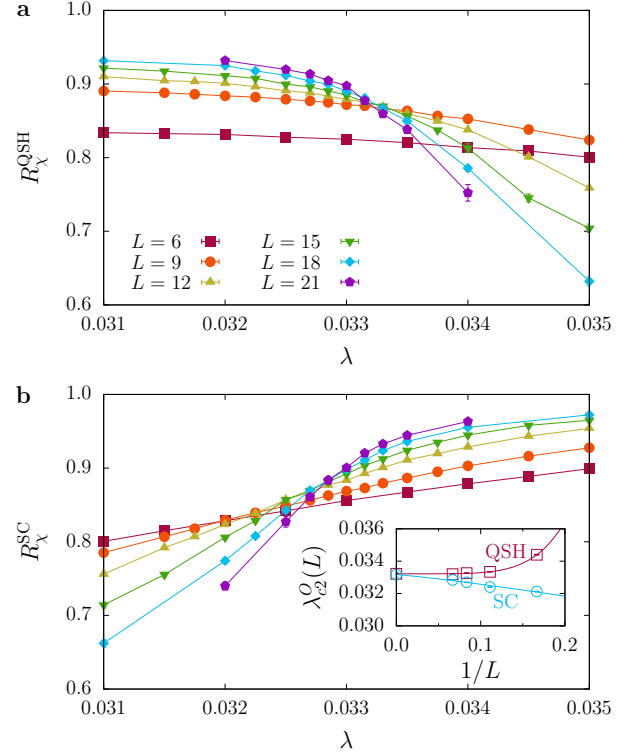


FIG. 3. Deconfined QSH-SC transition. **a** Correlation ratio R_χ^{QSH} and **b** correlation ratio R_χ^{SC} for different system sizes L . The extrapolation of the crossing points for L and $L + 6$ using the form $a + b/L^c$ (see inset of **b**) gives $\lambda_{c2}^{\text{QSH}} = 0.03322(3)$ and $\lambda_{c2}^{\text{SC}} = 0.0332(2)$.

The observed s-wave symmetry of the SC state emerges directly from the perspective of Dirac mass terms. In 2+1 dimensions and for $N = 8$ Dirac fermions, there exist numerous quintuplets of anti-commuting mass terms that combine different order parameters in a higher $\text{SO}(5)$ symmetry group.³² A well-known example relevant for DQCPs are the three AFM and two VBS mass terms. The three QSH mass terms form a quintuplet with the two s-wave SC mass terms. The resulting $\text{SO}(5)$ order parameter allows for a very natural derivation of the Wess-Zumino-Witten term,^{33,34} crucial for the DQCP, by integrating out the (massive) Dirac fermions.³⁵

As argued in the introduction, the QSH-SC problem is free of monopoles, so that our lattice model represents an improved model to study the DQCP. Although simulations for fermions are limited to smaller system sizes than for bosons, severe size effects due to monopoles¹⁰ can be expected to be absent. Fig 4 shows a finite-size analysis for the correlation length exponent and the anomalous dimension, as obtained either from the QSH or the SC correlation ratio. The resulting estimates $\eta^{\text{QSH}} = 0.21(5)$ and $\eta^{\text{SC}} = 0.22(6)$ compare favourably with those from loop models¹¹ where $\eta^{\text{AFM}} = 0.259(6)$ and $\eta^{\text{VBS}} = 0.25(3)$. An alternative analysis in the sup-

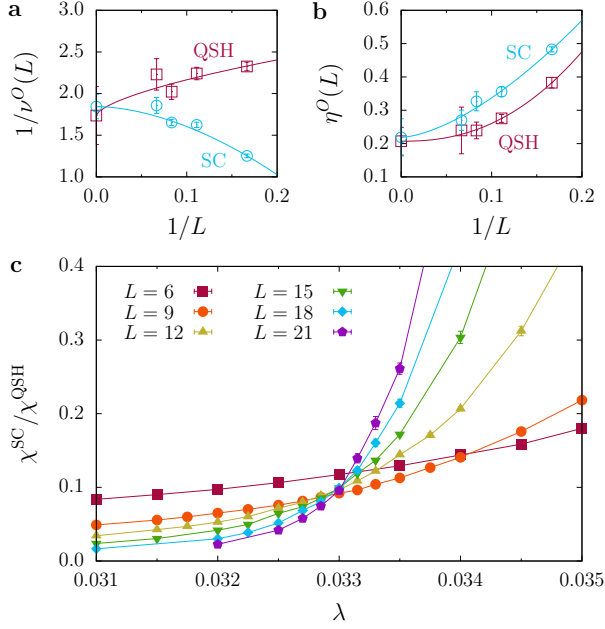


FIG. 4. **Critical exponents for the QSH-SC transition.** **a, b** Critical exponents $1/\nu^{SC} = 1.8(2)$, $1/\nu^{QSH} = 1.7(4)$, $\eta^{SC} = 0.22(6)$, and $\eta^{QSH} = 0.21(5)$ from finite-size scaling of the crossing points for L and $L + 6$. **c** Ratio of the QSH and SC susceptibilities for different system sizes L .

plementary material yields similar values. Given the very similar anomalous dimensions η^{QSH} and η^{SC} of QSH and SC fluctuations, the ratio of the QSH and SC susceptibilities is expected to be a renormalization group invariant, as confirmed by Fig. 4c. However, a crossing of different curves at λ_{c2} is a necessary but not sufficient condition for an emergent $SO(5)$ symmetry at the DQCP. In fact, a continuous transition with emergent $SO(5)$ symmetry can be essentially excluded here in the light of the condition $\eta > 0.52$ from the conformal bootstrap method.³⁶ The latter also yields a bound of $1/\nu < 1.957$ for a unitary conformal field theory with only one tuning parameter³⁷ that is satisfied by $1/\nu^{SC} = 1.8(2)$ and $1/\nu^{QSH} = 1.7(4)$ from Fig. 4a but not by $1/\nu = 2.24(4)$.¹⁰ Simulations of the monopole-free model on even larger lattices are required for a conclusive answer.

Our model provides a realisation of a QSH insulator emerging from spontaneous symmetry breaking. The corresponding $SO(3)$ order parameter permits both long-wavelength Goldstone modes and topological skyrmion defects. By means of a single parameter λ , we can trigger continuous quantum phase transitions to either a semimetal or an s-wave SC state. For the semimetal-QSH transition, the critical exponents are consistent with Gross-Neveu universality.^{28,29} The QSH-SC transition is of particular interest since it provides a monopole-free, improved model of deconfined quantum criticality with only one length scale. The mechanism for SC order

from the QSH state is the condensation of skyrmion defects of the QSH order parameter with charge $2e$. For the QSH-SC transition, our values of the anomalous dimension match those of previous work on the AFM-VBS transition,^{11,14} which are inconsistent with results from conformal bootstrap studies if an $SO(5)$ symmetry emerges at the critical point (as is supported by numerical and analytical studies). One possible resolution is the scenario of ‘pseudo-criticality’ or ‘walking coupling constant’.^{9,11,38,39} In contrast, our estimate of $1/\nu$ is still within the conformal bootstrap bound,³⁷ although a bound-violating result is not completely ruled out given the numerical uncertainty. Consequently, it is of considerable interest to exploit the full potential of quantum Monte Carlo methods in order to access even larger lattices. Other promising approaches that can shed further light on DQCPs make use of a lattice discretisation scheme based on projection onto a Landau level that does not break continuum symmetries.⁴⁰

A monopole-free realisation of DQCPs is impossible in traditional settings because of an anomaly⁹ associated with the $SO(3) \times U(1)$ symmetry. In the standard realisation, this anomaly is matched by the non-onsite nature of lattice rotation symmetries,⁴¹ but since lattice rotations are discrete, monopoles can never be completely suppressed. Alternatively, the anomaly can be eliminated by properly enlarging the $SO(3) \times U(1)$ symmetry, essentially allowing microscopic degrees of freedom that carry ‘fractional’ symmetry quantum numbers. This is what is being done in this work, where the fermions carry half-spin and half-charge (in terms of Cooper pair charges). An even simpler extension of the symmetry that eliminates the anomaly is $SU(2) \times U(1)$, meaning that microscopically there are charged spinless bosons, together with both charged and neutral spin-1/2 bosons. A challenge for future studies is to find a reasonably simple Hamiltonian that realises a DQCP and is amenable to sign-free bosonic QMC simulations in, e.g., the stochastic series expansion representation.⁴²

The SC phase generated from skyrmion defects motivates further investigations. Its vortex excitations carry a spin-1/2 degree of freedom,⁶ so that in the quantum critical fan thermal melting will yield a spin liquid.⁴³ It is also possible to add an independent attractive Hubbard interaction to explore a semimetal-QSH-SC tricritical point (as opposed to the recently discovered semimetal-AFM-VBS tricritical point²¹) with predicted $SO(5)$ Gross-Neveu criticality.⁴⁴ The vector form of \hat{H}_λ makes it straight forward to reduce the $SO(3)$ QSH symmetry to $U(1)$ and thereby investigate easy-plane realisation of DQCPs with a $U(1) \times U(1)$ symmetry on the lattice. Work along these directions is in progress.

Methods

We employed the ALF⁴⁵ implementation of the auxiliary-field finite-temperature quantum Monte Carlo method.^{23–25} The interaction term is written as a perfect square with negative prefactor ($\lambda > 0$), allowing for a decomposition in terms of a real Hubbard-Stratonovich field. For each field configuration, time-reversal symmetry holds and the eigenvalues of the fermion matrix occur in complex conjugate pairs.^{46–48} At low temperatures, the scales of the imaginary time propagation do not fit into double precision real numbers and we have used methods to circumvent this issue.⁴⁹ The imaginary-time discretisation was $\Delta\tau = 0.2$. For reasons explained in the supplementary material, we chose a symmetric Trotter decomposition that minimises discretization errors.

Acknowledgements

We acknowledge illuminating discussions with T. Grover, and with J. Hofmann regarding extensions of the ALF⁴⁵ package. We thank the Gauss Centre for Supercomputing (SuperMUC at the Leibniz Supercomputing Centre) for generous allocation of supercomputing resources as well as financial support from the Deutsche Forschungsgemeinschaft (DFG) grant AS120/14-1 for further development of the ALF package. TS thanks the DFG for financial support from grant number AS120/15-1. MH and ZW are supported by the DFG collaborative research centre SFB1170 ToCoTronics (project C01), YL and WG by NSFC under grants nos. 11775021 and 11734002. Research at Perimeter Institute (CW) is supported by the Government of Canada through the Department of Innovation, Science and Economic Development Canada and by the Province of Ontario through the Ministry of Research, Innovation and Science.

Author contributions

CW, WG and FFA conceived the project. YL and ZW implemented the model in the ALF package and carried out the simulations under the guidance of TS and MH. All authors participated in the interpretation of the results and the writing of the manuscript.

Competing financial interests

The authors declare no competing financial interests.

- [1] Kane, C. L. & Mele, E. J. Z_2 Topological Order and the Quantum Spin Hall Effect. *Phys. Rev. Lett.* **95**, 146802 (2005).
- [2] Raghu, S., Qi, X.-L., Honerkamp, C. & Zhang, S.-C. Topological Mott Insulators. *Phys. Rev. Lett.* **100**, 156401 (2008).
- [3] König, M. *et al.* Quantum Spin Hall Insulator State in HgTe Quantum Wells. *Science* **318**, 766 (2007).
- [4] Reis, F. *et al.* Bismuthene on a SiC substrate: A candidate for a high-temperature quantum spin Hall material. *Science* (2017).
- [5] Gross, D. J. & Neveu, A. Dynamical symmetry breaking in asymptotically free field theories. *Phys. Rev. D* **10**, 3235–3253 (1974).
- [6] Grover, T. & Senthil, T. Topological Spin Hall States, Charged Skyrmions, and Superconductivity in Two Dimensions. *Phys. Rev. Lett.* **100**, 156804 (2008).
- [7] Senthil, T., Balents, L., Sachdev, S., Vishwanath, A. & Fisher, M. P. A. Quantum criticality beyond the Landau-Ginzburg-Wilson paradigm. *Phys. Rev. B* **70**, 144407 (2004).
- [8] Senthil, T., Vishwanath, A., Balents, L., Sachdev, S. & Fisher, M. P. A. Deconfined Quantum Critical Points. *Science* **303**, 1490–1494 (2004).
- [9] Wang, C., Nahum, A., Metlitski, M. A., Xu, C. & Senthil, T. Deconfined Quantum Critical Points: Symmetries and Dualities. *Phys. Rev. X* **7**, 031051 (2017).
- [10] Shao, H., Guo, W. & Sandvik, A. W. Quantum criticality with two length scales. *Science* **352**, 213–216 (2016).
- [11] Nahum, A., Chalker, J. T., Serna, P., Ortuño, M. & Somoza, A. M. Deconfined Quantum Criticality, Scaling Violations, and Classical Loop Models. *Phys. Rev. X* **5**, 041048 (2015).
- [12] Nahum, A., Serna, P., Chalker, J. T., Ortuño, M. & Somoza, A. M. Emergent $SO(5)$ Symmetry at the Néel to Valence-Bond-Solid Transition. *Phys. Rev. Lett.* **115**, 267203 (2015).
- [13] Kawashima, N. & Tanabe, Y. Ground States of the $SU(N)$ Heisenberg Model. *Phys. Rev. Lett.* **98**, 057202 (2007).
- [14] Sandvik, A. W. Evidence for Deconfined Quantum Criticality in a Two-Dimensional Heisenberg Model with Four-Spin Interactions. *Phys. Rev. Lett.* **98**, 227202 (2007).
- [15] Berg, E., Metlitski, M. A. & Sachdev, S. Sign-Problem-Free Quantum Monte Carlo of the Onset of Antiferromagnetism in Metals. *Science* **338**, 1606–1609 (2012).
- [16] Kaul, R. K., Melko, R. G. & Sandvik, A. W. Bridging Lattice-Scale Physics and Continuum Field Theory with Quantum Monte Carlo Simulations. *Annual Review of Condensed Matter Physics* **4**, 179–215 (2013).
- [17] Xu, X. Y., Sun, K., Schattner, Y., Berg, E. & Meng, Z. Y. Non-Fermi Liquid at $(2+1)D$ Ferromagnetic Quantum Critical Point. *Phys. Rev. X* **7**, 031058 (2017).
- [18] Assaad, F. F. & Grover, T. Simple Fermionic Model of Deconfined Phases and Phase Transitions. *Phys. Rev. X* **6**, 041049 (2016).
- [19] Gazit, S., Randeria, M. & Vishwanath, A. Emergent Dirac fermions and broken symmetries in confined and deconfined phases of Z_2 gauge theories. *Nat. Phys.* **13**, 484–490 (2017).

- [20] Gazit, S., Assaad, F. F., Sachdev, S., Vishwanath, A. & Wang, C. Confinement transition of Z2 gauge theories coupled to massless fermions: Emergent quantum chromodynamics and SO(5) symmetry. *Proceedings of the National Academy of Sciences* (2018).
- [21] Sato, T., Hohenadler, M. & Assaad, F. F. Dirac Fermions with Competing Orders: Non-Landau Transition with Emergent Symmetry. *Phys. Rev. Lett.* **119**, 197203 (2017).
- [22] Novoselov, K. S. *et al.* Two-dimensional gas of massless Dirac fermions in graphene. *Nature* **438**, 197–200 (2005).
- [23] Blankenbecler, R., Scalapino, D. J. & Sugar, R. L. Monte Carlo calculations of coupled boson-fermion systems. *Phys. Rev. D* **24**, 2278–2286 (1981).
- [24] White, S. *et al.* Numerical study of the two-dimensional Hubbard model. *Phys. Rev. B* **40**, 506–516 (1989).
- [25] Assaad, F. & Evertz, H. World-line and Determinantal Quantum Monte Carlo Methods for Spins, Phonons and Electrons. In Fehske, H., Schneider, R. & Weiße, A. (eds.) *Computational Many-Particle Physics*, vol. 739 of *Lecture Notes in Physics*, 277–356 (Springer, Berlin Heidelberg, 2008).
- [26] Capponi, S. & Assaad, F. F. Spin-nematic phases in models of correlated electron systems: A numerical study. *Phys. Rev. B* **75**, 045115 (2007).
- [27] Herbut, I. F., Juričić, V. & Roy, B. Theory of interacting electrons on the honeycomb lattice. *Phys. Rev. B* **79**, 085116 (2009).
- [28] Parisen Toldin, F., Hohenadler, M., Assaad, F. F. & Herbut, I. F. Fermionic quantum criticality in honeycomb and π -flux Hubbard models: Finite-size scaling of renormalization-group-invariant observables from quantum Monte Carlo. *Phys. Rev. B* **91**, 165108 (2015).
- [29] Otsuka, Y., Yunoki, S. & Sorella, S. Universal Quantum Criticality in the Metal-Insulator Transition of Two-Dimensional Interacting Dirac Electrons. *Phys. Rev. X* **6**, 011029 (2016).
- [30] Zerf, N., Mihaila, L. N., Marquard, P., Herbut, I. F. & Scherer, M. M. Four-loop critical exponents for the Gross-Neveu-Yukawa models. *Phys. Rev. D* **96**, 096010 (2017).
- [31] Assaad, F. F. & Herbut, I. F. Pinning the Order: The Nature of Quantum Criticality in the Hubbard Model on Honeycomb Lattice. *Phys. Rev. X* **3**, 031010 (2013).
- [32] Ryu, S., Mudry, C., Hou, C.-Y. & Chamon, C. Masses in graphenelike two-dimensional electronic systems: Topological defects in order parameters and their fractional exchange statistics. *Phys. Rev. B* **80**, 205319 (2009).
- [33] Abanov, A. & Wiegmann, P. Theta-terms in nonlinear sigma-models. *Nuclear Physics B* **570**, 685 – 698 (2000).
- [34] Tanaka, A. & Hu, X. Many-Body Spin Berry Phases Emerging from the π -Flux State: Competition between Antiferromagnetism and the Valence-Bond-Solid State. *Phys. Rev. Lett.* **95**, 036402 (2005).
- [35] Senthil, T. & Fisher, M. P. A. Competing orders, non-linear sigma models, and topological terms in quantum magnets. *Phys. Rev. B* **74**, 064405 (2006).
- [36] Poland, D., Rychkov, S. & Vichi, A. The Conformal Bootstrap: Numerical Techniques and Applications. *ArXiv:1805.04405* (2018).
- [37] Nakayama, Y. & Ohtsuki, T. Necessary Condition for Emergent Symmetry from the Conformal Bootstrap. *Phys. Rev. Lett.* **117**, 131601 (2016).
- [38] Kuklov, A. B., Matsumoto, M., Prokof'ev, N. V., Svistunov, B. V. & Troyer, M. Deconfined Criticality: Generic First-Order Transition in the SU(2) Symmetry Case. *Phys. Rev. Lett.* **101**, 050405 (2008).
- [39] Gorbenco, V., Rychkov, S. & Zan, B. Walking, Weak first-order transitions, and Complex CFTs. *ArXiv e-prints* (2018).
- [40] Ippoliti, M., Mong, R. S. K., Assaad, F. F. & Zaletel, M. P. Half-filled Landau levels: a continuum and sign-free regularization for 3D quantum critical points. *ArXiv:1810.00009* (2018).
- [41] Metlitski, M. A. & Thorngren, R. Intrinsic and emergent anomalies at deconfined critical points. *Phys. Rev. B* **98**, 085140 (2018).
- [42] Sandvik, A. W. Stochastic series expansion method with operator-loop update. *Phys. Rev. B* **59**, R14157–R14160 (1999).
- [43] Sandvik, A. W., Kotov, V. N. & Sushkov, O. P. Thermodynamics of a Gas of Deconfined Bosonic Spinons in Two Dimensions. *Phys. Rev. Lett.* **106**, 207203 (2011).
- [44] Janssen, L., Herbut, I. F. & Scherer, M. M. Compatible orders and fermion-induced emergent symmetry in Dirac systems. *Phys. Rev. B* **97**, 041117 (2018).
- [45] Bercx, M., Goth, F., Hofmann, J. S. & Assaad, F. F. The ALF (Algorithms for Lattice Fermions) project release 1.0. Documentation for the auxiliary field quantum Monte Carlo code. *SciPost Phys.* **3**, 013 (2017).
- [46] Wu, C. & Zhang, S.-C. Sufficient condition for absence of the sign problem in the fermionic quantum Monte Carlo algorithm. *Phys. Rev. B* **71**, 155115 (2005).
- [47] Li, Z.-X., Jiang, Y.-F. & Yao, H. Majorana-Time-Reversal Symmetries: A Fundamental Principle for Sign-Problem-Free Quantum Monte Carlo Simulations. *Phys. Rev. Lett.* **117**, 267002 (2016).
- [48] Wei, Z. C., Wu, C., Li, Y., Zhang, S. & Xiang, T. Majorana Positivity and the Fermion Sign Problem of Quantum Monte Carlo Simulations. *Phys. Rev. Lett.* **116**, 250601 (2016).
- [49] Hofmann, J. S., Assaad, F. F. & Grover, T. Kondo Breakdown via Fractionalization in a Frustrated Kondo Lattice Model. *ArXiv:1807.08202* (2018).

SUPPLEMENTAL MATERIAL

Observables

Symmetry-broken states are characterised by a local order parameter $\hat{\mathbf{O}}_{\mathbf{r},\delta}$, where \mathbf{r} denotes a unit cell and δ an orbital within the unit cell. The associated time-displaced correlation functions read

$$S_{\delta,\delta'}^O(\mathbf{q}, \tau) = \frac{1}{L^2} \sum_{\mathbf{r}, \mathbf{r}'} \langle \hat{\mathbf{O}}_{\mathbf{r},\delta}(\tau) \cdot \hat{\mathbf{O}}_{\mathbf{r}',\delta'}(0) \rangle e^{i\mathbf{q} \cdot (\mathbf{r} - \mathbf{r}')} . \quad (8)$$

For the finite-size scaling analysis, we consider the order parameter

$$m^O = \sqrt{\frac{\Lambda_1(S_{\delta,\delta'}^O(\mathbf{0}, 0))}{L^2}} , \quad (9)$$

the equal-time correlation ratios

$$R^O = 1 - \frac{\Lambda_1(S_{\delta,\delta'}^O(\Delta\mathbf{q}, 0))}{\Lambda_1(S_{\delta,\delta'}^O(\mathbf{0}, 0))} , \quad (10)$$

with $|\Delta\mathbf{q}| = \frac{4\pi}{\sqrt{3}L}$, the susceptibilities

$$\chi^O = \Lambda_1 \left(\int_0^\beta d\tau S_{\delta,\delta'}^O(\mathbf{0}, \tau) \right) , \quad (11)$$

and the corresponding correlation ratios

$$R_\chi^O = 1 - \frac{\Lambda_1 \left(\int_0^\beta d\tau S_{\delta,\delta'}^O(\Delta\mathbf{q}, \tau) \right)}{\Lambda_1 \left(\int_0^\beta d\tau S_{\delta,\delta'}^O(\mathbf{0}, \tau) \right)} . \quad (12)$$

Here, $\Lambda_1()$ indicates the largest eigenvalue of the corresponding matrix in orbital space (6×6 for spin currents, 2×2 for pairing) and the ordering wave vector is at the Γ point.

These quantities exhibit the following finite-size scaling behaviour near the critical point:

$$\begin{aligned} m^O(L, \lambda) &= L^{(2-d-z-\eta)/2} f_1(L^z/\beta, (\lambda - \lambda_c)L^{1/\nu}, L^{-\omega_1}) , \\ R^O(L, \lambda) &= f_2(L^z/\beta, (\lambda - \lambda_c)L^{1/\nu}, L^{-\omega_2}) , \\ \chi^O(L, \lambda) &= L^{2-\eta} f_3(L^z/\beta, (\lambda - \lambda_c)L^{1/\nu}, L^{-\omega_3}) , \\ R_\chi^O(L, \lambda) &= f_4(L^z/\beta, (\lambda - \lambda_c)L^{1/\nu}, L^{-\omega_4}) . \end{aligned} \quad (13)$$

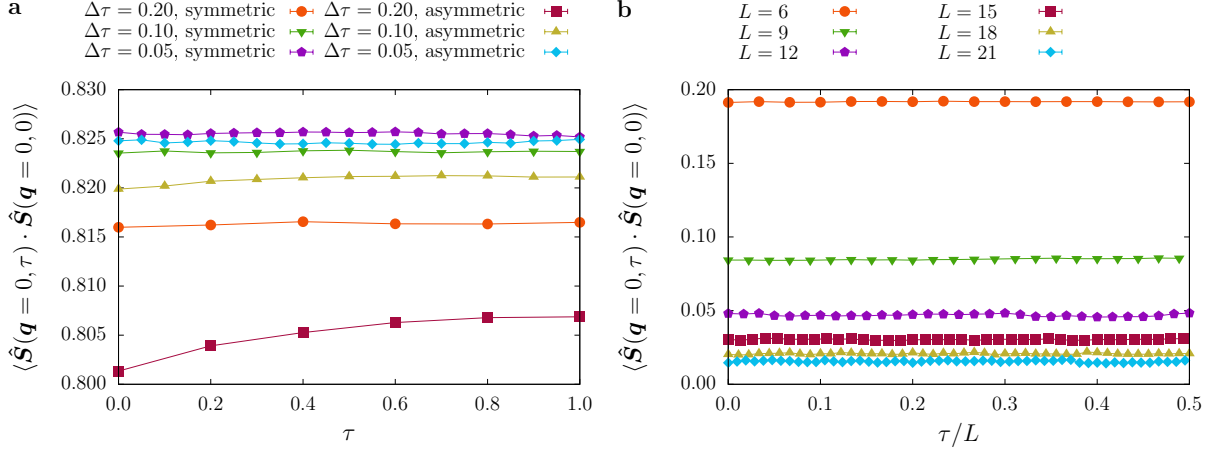
Here, λ_c, ν, η , and z are the critical coupling, the correlation length exponent, the anomalous dimension, and the dynamical critical exponent, respectively.

The correlation ratios R^O and R_χ^O are both renormalization group (RG) invariant quantities at the critical point and hence provide a simple way to estimate λ_c and ν without any knowledge about η . However, the generic corrections-to-scaling exponent ω is not necessarily the same for all four quantities in equation (13). Such corrections generally arise from irrelevant operators of the fixed point and the analytic part of the free energy. If the absolute value of the negative RG dimension is relatively large, the main contribution to ω will come from the background term of the free energy.²⁸ In this case,

$$\omega_1 = \omega_2 = 2 - z - \eta, \quad \omega_3 = \omega_4 = 2 - \eta . \quad (14)$$

This suggests that the susceptibility χ and the corresponding correlation ratio R_χ will have smaller scaling corrections than the corresponding equal-time quantities if the effect of the negative RG dimension is small at λ_c .

We assumed a dynamical critical exponent $z = 1$ for both the SM-QSH and the QSH-SC transition. This is motivated by the Lorentz invariance of the corresponding field theories.^{5,8} Accordingly, in our simulations, we used $\beta = L$ and thereby fixed L^z/β in the above finite-size scaling expressions.



S. Fig. 1. **a** Time-displaced spin correlation function at $\lambda = 0.04$, $\beta = 2$, and $L = 3$. The label ‘symmetric’ refers to the Trotter decomposition of equation (15), whereas ‘asymmetric’ refers to the alternative decomposition $Z = \text{Tr} \left[e^{-\Delta\tau \hat{H}_t} \left(\prod_{i=1}^N e^{-\Delta\tau \hat{H}_\lambda^x(i)} e^{-\Delta\tau \hat{H}_\lambda^y(i)} e^{-\Delta\tau \hat{H}_\lambda^z(i)} \right) \right]$. **b** Time-displaced spin correlation function for the symmetric Trotter decomposition and $\lambda = 0.019$, $\beta = L$.

Trotter decomposition used for the QMC simulations

For the finite-temperature QMC simulations underlying this work, imaginary time was discretized with a spacing $\Delta\tau = \beta/L_\tau$. To ensure hermiticity, the partition function is written as

$$Z = \text{Tr} \left[e^{-\frac{\Delta\tau}{2} \hat{H}_t} \left(\prod_{i=1}^N e^{-\frac{\Delta\tau}{2} \hat{H}_\lambda^x(i)} e^{-\frac{\Delta\tau}{2} \hat{H}_\lambda^y(i)} e^{-\frac{\Delta\tau}{2} \hat{H}_\lambda^z(i)} \prod_{j=N}^1 e^{-\frac{\Delta\tau}{2} \hat{H}_\lambda^z(j)} e^{-\frac{\Delta\tau}{2} \hat{H}_\lambda^y(j)} e^{-\frac{\Delta\tau}{2} \hat{H}_\lambda^x(j)} \right) e^{-\frac{\Delta\tau}{2} \hat{H}_t} \right]^{L_\tau} \quad (15)$$

where \hat{H}_t is defined by equation (1) and the interaction (2) was partitioned into local operators $H_\lambda^\alpha(i)$ acting on spin component $\alpha = x, y, z$ and on hexagon i . The leading discretization error for the partition function then scales as $\Delta\tau^2$.

The Trotter decomposition in equation (15) breaks the global $\text{SU}(2)$ spin rotation symmetry. For example, $[\hat{H}_\lambda^x(i), \hat{H}_\lambda^y(i)] \neq 0$, so that equation (15) will not be invariant under a global $\text{SU}(2)$ rotation. Because $\text{SU}(2)$ symmetry breaking is a relevant perturbation for both critical points considered, care has to be taken to ensure that its effects, which scale as $\Delta\tau^2$, remain below the relevant energy scale. An explicit test involves the total spin operator and generator of global $\text{SU}(2)$ rotations

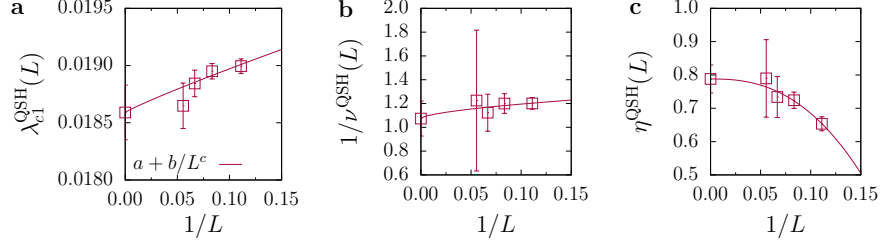
$$\mathbf{S}_{\text{tot}} = \frac{1}{L} \sum_{\mathbf{r}, \delta} \mathbf{S}_{\mathbf{r}, \delta}. \quad (16)$$

Here, $\mathbf{S}_{\mathbf{r}, \delta} = \hat{\mathbf{c}}_{\mathbf{r}+\delta}^\dagger \boldsymbol{\sigma} \mathbf{c}_{\mathbf{r}+\delta}$ and δ runs over the positions of atoms in the unit cell at \mathbf{r} . S.Fig 1 shows the associated time-displaced spin-spin correlation function. A global $\text{SU}(2)$ spin symmetry implies that this quantity is independent of imaginary time. The numerical results are essentially constant in imaginary time if the symmetric Trotter decomposition is used. Therefore, the latter was employed together with $\Delta\tau = 0.2$ for all results of this work.

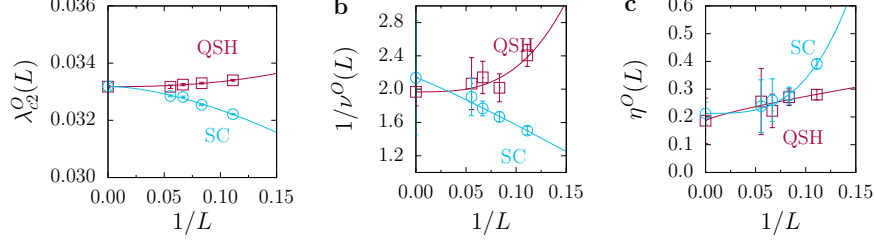
Finite-size scaling analysis by different crossing points

In addition to the main text, where a ‘two-size crossing’ with sizes L and $L+6$ was performed, we provide a cross check based on crossings of L and $L+3$.

When considering the L and $L+6$ crossings in the main text for the estimation of λ_{c2}^{SC} (see Fig. 3 of the main text), we are obliged to take into account the $L=6$ data. Upon inspection, the fit turns out to be rather bad since $\chi^2/\text{DOF} = 66.9$. On the other hand, if we consider the L and $L+3$ crossing points, we can omit the $L=6$ data and



S. Fig. 2. **Gross-Neveu semimetal-QSH transition.** **a** Extrapolation of the crossing points of R_χ^{QSH} for L and $L+3$ gives the critical value $\lambda_{c1}^{\text{QSH}} = 0.0186(3)$. **b** The inverse correlation length exponent $1/\nu^{\text{QSH}} = 1.1(2)$. **c** Estimation of the anomalous dimension $\eta^{\text{QSH}} = 0.79(5)$.



S. Fig. 3. **Deconfined QSH-SC transition.** **a** Estimation of the critical values $\lambda_{c2}^{\text{QSH}} = 0.03317(4)$ and $\lambda_{c2}^{\text{SC}} = 0.0332(1)$. **b,c** Critical exponents $1/\nu^{\text{SC}} = 2.1(7)$, $1/\nu^{\text{QSH}} = 2.0(2)$, $\eta^{\text{SC}} = 0.21(5)$, and $\eta^{\text{QSH}} = 0.19(9)$ from finite-size scaling of the crossing points of L and $L+3$.

get a more acceptable $\chi^2/\text{DOF} = 6.8$. As apparent from S.Fig. 3, the extrapolated value of λ_{c2}^{SC} based on the crossing points of L and $L+3$ compares favourably with the analysis in the main text.

S.Fig 2a,b show the crossing values of λ and $1/\nu$ at the semimetal-QSH transition, as obtained from the correlation ratio. S.Fig 2 c shows the anomalous dimension η at each crossing point, as well as a fit based on an expression analogous to Eq. (6) of the main text,

$$\eta^O(L) = 2 - \frac{1}{\log r} \log \left(\frac{\chi^O(\lambda, rL)}{\chi^O(\lambda, L)} \right) \Big|_{\lambda=\lambda_c^O(L)}, \quad (17)$$

where $r = \frac{L+3}{L}$.

The results of a similar analysis for the QSH-SC transition are reported in S.Fig. 3.

Consistency of the finite-size scaling analysis

As an independent consistency check on the results from the ‘two-size crossing’ method used in the main text, we consider in this section a collective fitting of multiple system sizes.

The collective fitting of λ_c and ν is based on a polynomial expansion of the scaling function of $R_\chi^O(L, \lambda)$ in equation (13). Taking $\beta = L$, we have

$$R_\chi^O(L, \lambda) \approx \sum_{p=0}^n a_p (\lambda - \lambda_c)^p L^{p/\nu} + L^{-\omega} \sum_{q=0}^m b_q (\lambda - \lambda_c)^q L^{q/\nu}. \quad (18)$$

Here, n and m are the expansion orders for the dimensionless and the scaling correction part of the universal function, respectively.

Table I reports the results of fits for the two order parameters at the DQCP, including the case with $m = 1$, as well as the case without considering any scaling correction. We set $n = 2$ for all the fits. For $m = 1$, the fitting of the QSH correlation ratio is satisfactory in terms of χ^2/DOF for $L_{\min} \geq 9$, and the results are consistent with each other for $L_{\min} = 9, 12, 15$. Taking $\lambda_{c2} = 0.03314(5)$ and $1/\nu = 1.55(9)$ from the fit with $L_{\min} = 9$, we get consistency with $\lambda_{c2}^{\text{QSH}} = 0.03322(3)$ and $1/\nu^{\text{QSH}} = 1.7(4)$ from the ‘two-size crossing’ analysis in the main text. The results of

DQCP – QSH						DQCP – SC					
L_{\min}	λ_c	$R_{\chi}^{\text{QSH}}(\lambda_c)$	$1/\nu$	ω	χ^2/DOF	L_{\min}	λ_c	$R_{\chi}^{\text{SC}}(\lambda_c)$	$1/\nu$	ω	χ^2/DOF
9	0.03332(1)	0.8665(4)	2.22(5)	n/a	139/44	9	0.032675(4)	0.8592(4)	1.32(3)	n/a	1239/40
12	0.03326(2)	0.8702(8)	2.21(7)	n/a	58.9/32	12	0.032791(5)	0.8742(5)	1.60(4)	n/a	123/29
15	0.03326(3)	0.870(2)	2.3(2)	n/a	33.4/22	15	0.032843(8)	0.882(1)	1.83(6)	n/a	15.9/18
18	0.03321(5)	0.875(5)	2.4(3)	n/a	13.9/12	18	0.03286(3)	0.884(4)	1.9(2)	n/a	2.23/9
9	0.3314(5)	0.89(2)	1.55(9)	0.9(3)	29.1/41	9	0.03296(5)	0.907(9)	2.1(2)	1.7(3)	53.8/37
12	0.331(2)	0.92(9)	1.5(2)	0.4(9)	24.7/29	12	0.03287(2)	0.887(2)	2.3(2)	4.4(8)	26.0/26
15	0.331(2)	0.89(2)	1.6(3)	4(3)	15.1/19	15	0.0329(2)	0.89(3)	2.0(4)	3(13)	15.1/15
9	0.3315(5)	0.89(2)	1.5(2)	0.9(4)	28.2/36	9	0.0331(2)	0.94(4)	1.9(2)	1.1(5)	42.5/33
12	0.331(2)	0.91(8)	1.5(2)	0.5(9)	23.8/26	12	0.03285(3)	0.884(5)	2.0(3)	8(6)	20.6/22
15	0.331(2)	0.89(3)	1.7(3)	3(3)	13.9/16	15	0.0329(2)	0.89(3)	1.7(5)	4(16)	14.4/13

TABLE I. Collective fitting at the DQCP for λ_c , $1/\nu$, and $R_{\chi}^O(\lambda_c)$ based on the correlation ratios $R_{\chi}^O(L, \lambda)$ and equation (18). We compare the case without taking into account scaling corrections (data rows 1–4) to the case with $m = 1$ (rows 5–7 correspond to a larger data window, rows 8–10 to a smaller one); in both cases, $n = 2$.

DQCP – QSH			DQCP – SC		
L_{\min}	η	χ^2/DOF	L_{\min}	η	χ^2/DOF
6	0.30(2)	990/68	6	0.344(8)	525/45
9	0.24(1)	249/57	9	0.308(7)	128/36
12	0.19(2)	92.0/40	12	0.28(2)	65.6/26
15	0.24(3)	49.8/25	15	0.23(2)	24.2/17
18	0.18(6)	12.0/12	18	0.19(9)	7.47/8

TABLE II. Same analysis as in table I but for the exponent η using equation (19). Here $n = 2$, while scaling corrections are ignored.

a fit with a smaller data window are shown in the last three rows of table I, revealing that the results are stable upon variation of the number of degrees of freedom. A fit using R_{χ}^{SC} also produces acceptable values of χ^2/DOF for $L_{\min} = 9, 12$ and 15 and compares favourably with the results presented in the main text.

To reduce the number of degrees of freedom in the fit of the anomalous dimension η , a substitution in terms of the scaling form for χ^O and R_{χ}^O in equation (13) is performed, using the expansion (we ignore the correction-to-scaling term)

$$\chi^O(L, R) = L^{2-\eta} f(R) \approx L^{2-\eta} \sum_{p=0}^n a_p R^p. \quad (19)$$

As shown in table II, the collective fitting for both order parameters is acceptable for $L_{\min} \geq 12$. The corresponding values $\eta^{\text{QSH}} = 0.194(9)$ and $\eta^{\text{SC}} = 0.279(9)$ agree well with the values 0.21(5) and 0.22(6) obtained with the ‘two-size crossing’ approach used in the main text.

We also carried out the collective fitting at the Gross-Neveu critical point. In contrast to the DQCP, this phase transition suffers much less from corrections to scaling (as shown in Fig. 3 of the main text, the crossing points converge quickly). Hence, a fit without the scaling correction term is performed, and the results are shown in table III. As can be seen, a good χ^2/DOF is obtained once the $L = 6$ data set is neglected, and fits for $L_{\min} = 9, 12, 15$ or 18 produce consistent results. Taking $\lambda_{c1} = 0.01891(2)$ and $1/\nu = 1.17(3)$ from $L_{\min} = 9$, the results match those of the analysis in the main text.

Results for the anomalous dimension at the Gross-Neveu critical point are listed in table III. The fits yield acceptable χ^2 values for $L_{\min} \geq 12$. The exponent $\eta = 0.76(1)$ from $L_{\min} = 12$ also matches the analysis in the main text.

Gross-Neveu – QSH						Gross-Neveu – QSH		
L_{\min}	λ_c	$R_{\chi}^{\text{QSH}}(\lambda_c)$	$1/\nu$	ω	χ^2/DOF	L_{\min}	η	χ^2/DOF
6	0.01898(2)	0.6970(6)	1.26(2)	n/a	94.6/34	6	0.666(7)	210/33
9	0.01891(2)	0.693(1)	1.17(3)	n/a	34.8/27	9	0.70(1)	111/26
12	0.01882(4)	0.687(2)	1.17(5)	n/a	18.6/20	12	0.76(2)	28.6/18
15	0.01870(7)	0.678(5)	1.14(11)	n/a	9.22/13	15	0.78(2)	4.4/12
18	0.0186(2)	0.67(2)	1.3(4)	n/a	1.90/6	18	0.81(6)	1.9/6

TABLE III. Same as table I, but for the Gross-Neveu transition. Here $n = 2$, while scaling corrections are ignored.

Single-particle gap and free-energy derivative across the QSH-SC transition

The single-particle gap Δ_{sp} is obtained from the single-particle Green function

$$G(\mathbf{k}, \tau) = \frac{1}{L^2} \sum_{\mathbf{r}, \mathbf{r}', \delta, \sigma} \langle \hat{c}_{\mathbf{r}+\delta, \sigma}^\dagger(\tau) \hat{c}_{\mathbf{r}', \sigma}(0) \rangle e^{i\mathbf{k} \cdot (\mathbf{r} - \mathbf{r}')} \quad (20)$$

where $\mathbf{r} + \delta$ runs over the two orbitals of the unit cell located at \mathbf{r} . The single-particle gap is minimal at the Dirac point $\mathbf{K} = (\frac{4\pi}{3}, 0)$ and is extracted by noting that asymptotically

$$G(\mathbf{K}, \tau) \propto e^{-\Delta_{\text{sp}}\tau}. \quad (21)$$

Here, we used $\beta = 36$. S.Fig 4a demonstrates that Δ_{sp} remains nonzero across the QSH-SC transition at $\lambda_{c2} \approx 0.033$.

In order to clarify nature of the QSH-SC transition, we also calculated the first partial derivative of the free energy density with respect to the coupling λ (we use the same notation as in the main text)

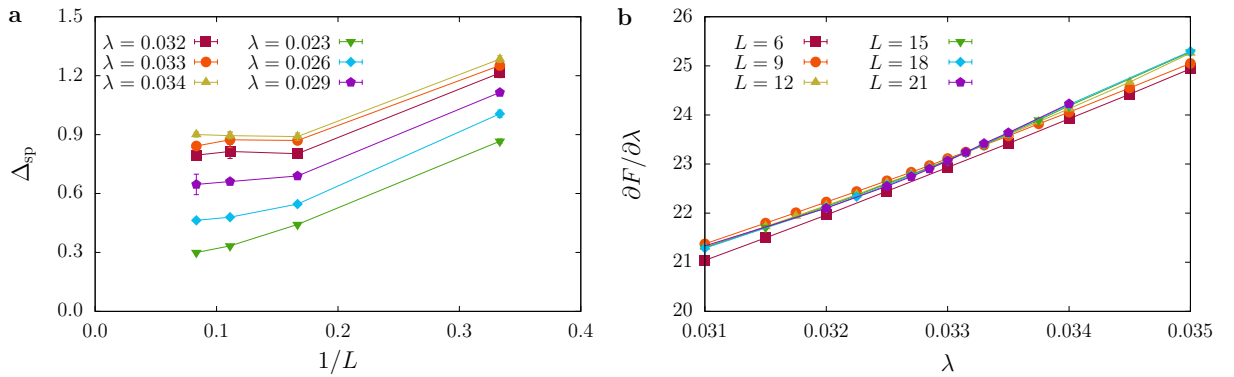
$$\frac{\partial F}{\partial \lambda} = -\frac{1}{L^2} \sum_{\square} \left\langle \left(\sum_{\langle \langle i, j \rangle \rangle \in \square} i\nu_{ij} \hat{c}_i^\dagger \sigma \hat{c}_j + \text{H.c.} \right)^2 \right\rangle. \quad (22)$$

S.Fig 4b shows $\partial F/\partial \lambda$ for $\beta = L$ in the vicinity of $\lambda_{c2} \approx 0.033$. As expected for a continuous transition, we observe no sign of a jump.

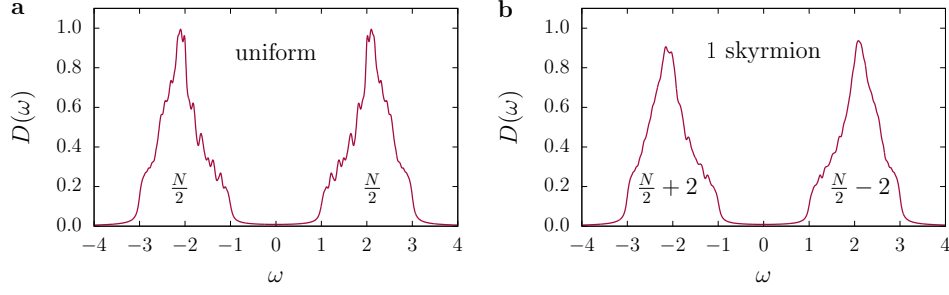
Charged skyrmion defects of the QSH state

In Ref.,⁶ it was shown that when a QSH state is generated by spontaneous symmetry breaking, skyrmion defects of the vector order parameter will carry an electric charge of $Q_e = 2e$, leading to the relation

$$Q_e = 2eQ \quad (23)$$



S. Fig. 4. **a** Fermionic single-particle gap and **b** free-energy derivative $\partial F/\partial \lambda$ across the QSH-SC transition at $\lambda_{c2}^{\text{SC}} = 0.0331(3)$.



S. Fig. 5. Density of states $N(\omega)$ of Hamiltonian (24) for **a** uniform polarisation, **b** a ‘single skyrmion’ configuration with $Q \approx -0.989$. We have included an artificial broadening by using the form $D(\omega) = -\pi^{-1} \sum_n \text{Im}(\omega - \varepsilon_n + i\delta)^{-1}$, where ε_n are the eigenvalues and $\delta = 0.05$. Here, $L = 36$, $\lambda = 0.5$.

where Q is the Pontryagin index that counts the winding of the unit vector order parameter on the sphere.

Here, we substantiate this fact in terms of an explicit calculation for a lattice model. Our starting point is the Hamiltonian

$$\hat{H} = -t \sum_{\langle \mathbf{i}, \mathbf{j} \rangle} (\hat{\mathbf{c}}_{\mathbf{i}}^\dagger \hat{\mathbf{c}}_{\mathbf{j}} + \text{H.c.}) + \lambda \sum_{\square} \mathbf{N}(\mathbf{x}) \cdot \left(\sum_{\langle \langle \mathbf{i}, \mathbf{j} \rangle \rangle \in \square} \underbrace{i\nu_{ij} \hat{\mathbf{c}}_{\mathbf{i}}^\dagger \boldsymbol{\sigma} \hat{\mathbf{c}}_{\mathbf{j}} + \text{H.c.}}_{\equiv \hat{\mathbf{J}}_{ij}} \right), \quad (24)$$

where $\mathbf{N}(\mathbf{x}) = (N^x(\mathbf{x}), N^y(\mathbf{x}), N^z(\mathbf{x}))$ is a unit vector at position \mathbf{x} corresponding to the centre of a hexagon. Since \hat{H} is invariant under time reversal symmetry, $\hat{T}^{-1} \alpha(\hat{\mathbf{c}}_{i,\uparrow}) \hat{T} = \bar{\alpha}(\hat{\mathbf{c}}_{i,\downarrow})$, Kramers’ theorem holds and stipulates that all eigenstates are doubly degenerate.

On the honeycomb lattice, the Pontryagin index is defined as

$$Q = \frac{1}{8\pi} \sum_{\mathbf{x}} \mathbf{N}(\mathbf{x}) \cdot (\mathbf{N}(\mathbf{x} + \mathbf{a}_1) - \mathbf{N}(\mathbf{x})) \times [(\mathbf{N}(\mathbf{x}) - \mathbf{N}(\mathbf{x} + \mathbf{a}_2)) + (\mathbf{N}(\mathbf{x}) - \mathbf{N}(\mathbf{x} - \mathbf{a}_1 + \mathbf{a}_2))] \quad (25)$$

with unit vectors $\mathbf{a}_1 = (1, 0)$ and $\mathbf{a}_2 = (\frac{1}{2}, \frac{\sqrt{3}}{2})$.

For an arbitrary vector field $\mathbf{N}(\mathbf{x})$, Hamiltonian (24) does not preserve particle-hole (P-H) symmetry. For example, defining the P-H transformation as

$$\hat{P}_z^{-1} \alpha \left(\begin{pmatrix} \hat{\mathbf{c}}_{i,\uparrow}^\dagger \\ \hat{\mathbf{c}}_{i,\downarrow}^\dagger \end{pmatrix} \right) \hat{P}_z = \eta_i \bar{\alpha} \left(\begin{pmatrix} \hat{\mathbf{c}}_{i,\uparrow} \\ -\hat{\mathbf{c}}_{i,\downarrow} \end{pmatrix} \right), \quad (26)$$

where $\eta_i = 1 (-1)$ for $i \in \text{A (B)}$, we have

$$\begin{aligned} \hat{P}_z^{-1} \hat{J}_{i,j}^x \hat{P}_z &= \hat{J}_{i,j}^x, \\ \hat{P}_z^{-1} \hat{J}_{i,j}^y \hat{P}_z &= \hat{J}_{i,j}^y, \\ \hat{P}_z^{-1} \hat{J}_{i,j}^z \hat{P}_z &= -\hat{J}_{i,j}^z. \end{aligned} \quad (27)$$

A general P-H transformation can be written as

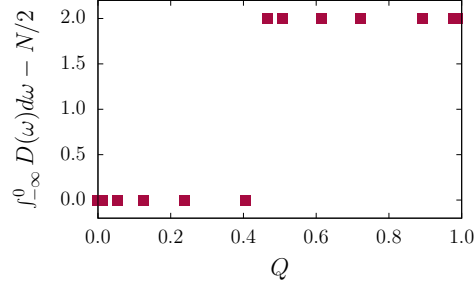
$$\hat{P}(\theta, \phi) = \hat{U}^{-1}(\theta, \phi) \hat{P}_z \hat{U}(\theta, \phi) \quad (28)$$

where

$$\hat{U}^{-1}(\theta, \phi) \begin{pmatrix} \hat{\mathbf{c}}_{i,\uparrow} \\ \hat{\mathbf{c}}_{i,\downarrow} \end{pmatrix} \hat{U}(\theta, \phi) = \begin{pmatrix} \cos(\theta/2) & -\sin(\theta/2)e^{-i\phi} \\ \sin(\theta/2)e^{i\phi} & \cos(\theta/2) \end{pmatrix} \begin{pmatrix} \hat{\mathbf{c}}_{i,\uparrow} \\ \hat{\mathbf{c}}_{i,\downarrow} \end{pmatrix}. \quad (29)$$

For Hamiltonian (24), it yields

$$\hat{P}^{-1}(\theta, \phi) \hat{H}(\mathbf{N}) \hat{P}(\theta, \phi) = H(\mathbf{N}') \quad (30)$$



S. Fig. 6. Integrated density of states as a function of Q for open boundary conditions and $L = 36$.

where

$$\mathbf{N}'(\mathbf{x}) = R^{-1}(\theta, \phi) \begin{pmatrix} 1 & 0 & 0 \\ 0 & 1 & 0 \\ 0 & 0 & -1 \end{pmatrix} R(\theta, \phi) \mathbf{N}(\mathbf{x}) \quad (31)$$

and

$$R(\theta, \phi) = \begin{pmatrix} \cos^2(\theta/2) - \sin^2(\theta/2) \cos(2\phi) & -\sin^2(\theta/2) \sin(2\phi) & -\sin(\theta) \cos(\phi) \\ -\sin^2(\theta/2) \sin(2\phi) & \cos^2(\theta/2) + \sin^2(\theta/2) \cos(2\phi) & -\sin(\theta) \sin(\phi) \\ \sin(\theta) \cos(\phi) & \sin(\theta) \sin(\phi) & \cos(\theta) \end{pmatrix}. \quad (32)$$

Thus, there is no generic P-H transformation that leaves this Hamiltonian invariant, unless $\mathbf{N}(\mathbf{x})$ is varied in an R^2 space (θ and ϕ can be defined such that $\sin \theta \cos \phi N_x + \sin \theta \sin \phi N_y + \cos \theta N_z = 0$). Since the transformation has a determinant of -1 , the generic P-H transformation gives

$$Q(\mathbf{N}'(\mathbf{x})) = -Q(\mathbf{N}(\mathbf{x})). \quad (33)$$

The ‘electric charge’ refers to the number of occupied states at zero temperature, relative to half filling. The sign change of the Pontryagin index under a P-H transformation provides a natural way of understanding equation (23). Note that in contrast to a skyrmion, a 2D topological defect (such as vortex) has a vanishing Pontryagin index and carries no charge.

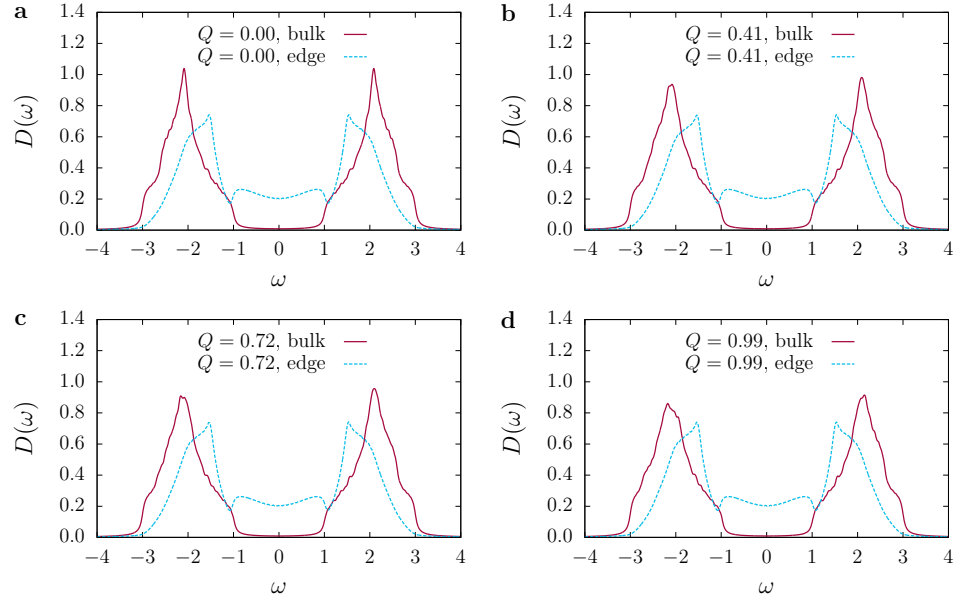
The argument of charged skyrmions fails when other Dirac mass terms are considered. For example, a system with fluctuations of a three component vector field Yukawa-coupled to the three antiferromagnetic mass terms does not break P-H symmetry. In this case, a skyrmion configuration with nonzero Pontryagin index does not carry electric charge.

We diagonalised Hamiltonian (24) on a honeycomb lattice with $L = 36$, setting $t = 1$ and $\lambda = 0.5$. S.Fig 5 compares the density of states for a uniform field $\mathbf{N}(\mathbf{x})$ and for a ‘hedgehog’ configuration corresponding to a single skyrmion. On the lattice, the Pontryagin index is not quantised and we obtain $Q \approx -0.989$. The system remains gapped when one skyrmion is inserted, see S.Fig. 5b. The breaking of P-H symmetry is also apparent from $D(\omega) \neq D(-\omega)$. Simple number counting shows that

$$\int_{-\infty}^0 D(\omega) d\omega = N/2 + 2, \quad \int_0^{\infty} D(\omega) d\omega = N/2 - 2. \quad (34)$$

Compared to the case of uniform polarisation in S.Fig. 5a, an additional charge $2e$ is generated.

On a system with open boundary conditions, the Pontryagin index is not necessarily quantised and we can investigate how charge is transferred during the *insertion* of a skyrmion by varying the Pontryagin index from zero to one. S.Fig 6 shows that the total charge is ‘pumped’ from 0 to $2e$ and we observe a step function at a non-integer value of Q . This is a consequence of the aforementioned Kramers theorem. As shown in S.Fig. 7, the bulk remains gapped during this process, while the edge stays gapless. Thus, the charge $2e$ is pumped through the edge under insertion of a skyrmion.



S. Fig. 7. Edge and bulk density of states for different $N(\mathbf{x})$, corresponding to the values of Q given in each panel. Here, $L = 36$, and $D(\omega)$ was broadened as explained in S.Fig. 5.